3D smooth particle hydrodynamics modeling for high velocity penetrating impact using GPU: Application to a blunt projectile penetrating thin steel plates

H. Frissane, L. Taddei, N. Lebaal, S. Roth

Version of Record: https://www.sciencedirect.com/science/article/pii/S004578251930461X
Manuscript_46e5fa79ba6ea5bbe3642c3dadf45eb4

3D smooth particle hydrodynamics modelling for high velocity penetrating impact using GPU: Application to a blunt projectile penetrating thin steel plates.

H. Frissane[a,*], L. Taddei[a], N. Lebaal[a], S. Roth[a]

[a]*Laboratoire Interdisciplinaire Carnot de Bourgogne/ Site UTBM, UMR CNRS 6303/ Univ. Bourgogne Franche Comté (UBFC), F-90010 Belfort, France*

Abstract

The high velocity impact (HVI) framework with or without penetration leads to considering several physical phenomena, such as large deformation, damage mechanics and rupture. Our understanding of these impacts can be approached by numerical simulation. In this paper, the penetration of thin metal plates struck by a blunt projectile is simulated using meshfree particle analysis and the smoothed particle hydrodynamics (SPH) method. The Johnson-Cook elastic-plastic model and the simplified damage model were applied to simulate the mechanical behaviour in this study. Penalty force algorithms were implemented in the model to manage the contact phenomenon. In addition, to overcome the computational cost, which is critical with SPH simulation, a developed solver graphics processing unit (GPU) was used. This enabled us to accelerate the simulation time and also allowed the use of large numbers of particles (2–8 million). The computational results were compared with experimental results published in the literature in terms of the ballistic curve in these plates.

Keywords: Ballistic penetration, Constitutive relations, Elastic-plastic behavior, Smoothed particle hydrodynamics, GPU.

1. Introduction

The penetration of projectiles into a target at high velocity impact (HVI) has been studied for many decades. This area of applied mechanics has been a subject of interest in aerospace, military, nuclear and civil engineering, among others. In the discipline of impact engineering, and for ballistic impact of a projectile against a mechanical structure, it is essential to understand their response to optimally design protecting structures. The literature includes numerous studies of many different impact configurations, including the effects of different parameters that influence the perforation and the ballistic performance of the target.

Numerous parameter effects have been of interest in the literature. Similar and contradictory observations in the literature have revealed that the influence of the projectile's nose shape in the structural impact is governed by parameters varying from one investigation to another. Therefore, systematic study and more investigation was necessary to determine the governing parameters of the influence of projectile nose shape on the ballistic performance of the target material (Børvik et al., 2002; Dey et al., 2007; Iqbal et al., 2012).

*Laboratoire Interdisciplinaire Carnot de Bourgogne/ Site UTBM, UMR CNRS 6303/ Univ. Bourgogne Franche Comté (UBFC), F-90010 Belfort, France. Tel.: +33 (0)3 84 58 20 16; Fax.: +33 (0)3 84 58 32 86.

Email address: hassan.frissane@utbm.fr (H. Frissane)

Another parameter that influences the ballistic performance of target material impacted by projectiles is the thickness of the target plate (Dey et al., 2007). Gupta et al. (2007) and Børvik et al. (2001b) found that the ballistic limit velocity of the target plate increased with increasing target plate thickness. Material strength has also played an important role on the penetration of projectiles. An experiment conducted by Børvik et al. (2009) revealed that the ballistic limit velocity increases with the increase of the yield strength of the target materials. However, Dey et al. (2004) found that the difference ballistic limit velocity of different target materials used were not significant for similar projectile nose shapes, although there were large differences between the yield strengths of the targets.

The so-called ideal collisions did not occur in a real case scenario. One of the non-ideal collisions that was described by Backman and Goldsmith (1978) was impact with angularity. It was observed that the angle of obliquity was another important parameter that affects the ballistic limit of the target. Investigation of the impacts problem is complex and expensive because it requires testing equipment, testing environment, testing prototypes, and testing configuration. The development of computational science allows us to develop efficient and reliable methods, which helps to overcome the issues linked to experiments. Finite Element Method (FEM) is one of the most classical numerical methods used to deal with dynamic problem. However, FEM suffers from a severe mesh distortion or mesh tangling problem when dealing with HVI problems (Belytschko and Lin, 1987; Johnson and Stryk, 1987). Consequently, a new particle meshfree method to solve the mesh problem such as the smoothed particle hydrodynamics (SPH) was developed in the literature. A particle meshfree method is appropriate when dealing with dynamics problems involving severe damages (Giannaros et al., 2019; Zhang and Liu, 2017). Some of the numerical investigations that dealt with this dynamic problem by adopting the mesh-free SPH can be found in the literature (Alhussan et al., 2012; Hayhurst and Clegg, 1997; Mehra and Chaturvedi, 2006; Swaddiwudhipong et al., 2010; Taddei et al., 2015; Vignjevic et al., 2004).

In the present study, a numerical method based on SPH was developed and applied to simulate thin plates of steel impacted by s blunt projectile (Børvik et al., 2003). The ultimate goal was to provide fundamental physical insight and derive a physics-based HVI model for a use in several simulation configurations. Although SPH is well suited to such problems, using a large model (perfectly SPH) with different material could lead to three important barriers. The first one concerns the number of particles included in the simulation, which can increase the computational time when increasing the number of particles. The second deals with the complexity of the calculation when the problems involve complex physical phenomenon (multiphase, complex material, etc.) (Colagrossi and Landrini, 2003). The third concerns 3D simulations, which are necessary to capture some physical phenomenon that are not axisymmetric (oblique ballistic impact). For this reason, a HVI 3D-SPH simulation need a small time step to respect CFL(Courant–Friedrichs–Lewy) condition and a large number of particles. All these points led to extreme time computation. To reduce computational runtimes, an operable option is to use a GPU. Due to the locality of SPH interactions, multiple component schemes require identification of neighboring particles. In impact simulations that involve, at least, two different bodies (with different mechanical characteristics), such as multiple component systems, the influence between different particle types leads to increase the time complexity, as well as the contact algorithm between different bodies. To solve this kind of problem, different GPU algorithms were reported, Zheng et al. (2012) including the uniform grid method and the study of Pabst et al. (2010), which used a spatial subdivision approach. In the framework in SPH development and despite their suitability for scientific computing, there has been only limited research and development using GPU. Crespo et al. (2011) and Hérault et al. (2010) initiated research using the GPU algorithm and compared with CPU implementation with significant improvement speedups for the GPU codes.

This paper presents a new approach to the development of GPU algorithms, combined to a 3D SPH

code, allowing us to simulate a complex HVI configuration. This paper is structured as follows: first, the governing equations are presented, as well as the SPH formulation implemented using GPU. The GPU algorithm for impact simulations is then presented using CUDA profiling data. Finally, the HVI-SPH GPU scheme is applied to 3D impact cases where the comparison between simulations and experiments of the literature are conducted and illustrated.

2. SPH: 3D formulation

The SPH method can be described in different steps, as follows: discretization of the domain, integration of the variables, replacement of the integration by summation in the support domain of all particles, and time integration. This method can solve problems where the governing partial differential equations describe the co-moving evolution of the density, coordinates, velocity, and energy per unit mass in terms of the velocity gradients, pressure tensor, and stress tensor. According to Lucy (1977) and Gingold and Monaghan (1977), the SPH interpolates the set of field variable by means of kernel interpolation. For any variable $f(\boldsymbol{q})$, a local average at each coordinate $\boldsymbol{q}_i$ is calculated according to Eq.(2.1)

$$\forall i \in \boldsymbol{K},\ \ \langle f\left(\boldsymbol{q_i}\right)\rangle = \int_{\boldsymbol{\Omega_i}} f W d\boldsymbol{\Omega} = \sum_{j\in \boldsymbol{K_i}} \frac{m_j}{\rho_j} f_j W\left(\|\boldsymbol{q}_{ij}\|_2, h\right), \tag{2.1}$$

where m_j, ρ_j, f_j and $\boldsymbol{\Omega_i}$ are, respectively, the mass of the particle j, the density, the value of the field $f(\boldsymbol{q})$ at position $\boldsymbol{q}_j$, and the compact support of a particle i and $\boldsymbol{q}_{ij} = \boldsymbol{q}_i - \boldsymbol{q}_j$. For the next, the notation, $a_{ij} = a_i - a_j$, $\overline{a}_{ij} = \frac{1}{2}(a_i + a_j)$, and $W\left(\|\boldsymbol{q}_{ij}\|_2, h\right) = W_{ij}$ are employed. W_{ij} is a kernel function, which is parameterized by the value h corresponding to the smoothing length. The sum in Eq. (2.1) formally extends over all particles. However, due to the compact support of W, only the particle of index $j \in K_i$ needs to be considered, where $\boldsymbol{K}_i = \{\ j \mid \|\boldsymbol{q}_{ij}\|_2 < 2h\}$ and $\boldsymbol{K} = \bigcup_{i=0}^{N} \boldsymbol{K}_i$, with N is the total number of particles.
A particularly convenient feature of SPH is that neither m_j nor f_j is affected by the gradient operator ∇. Because the m_j and f_j are themselves particle properties, the gradient operator affects only the weight function W_{ij}. Therefore, the gradient of a vector field $f(\boldsymbol{q})$, evaluated at position $\boldsymbol{q}_i$, is obtained as follows :

$$\forall i \in \boldsymbol{K},\ \ \langle \nabla f(\boldsymbol{q}_i)\rangle = \sum_{j\in \boldsymbol{K_i}} \frac{m_j}{\rho_j} f_j \nabla_i W_{ij}. \tag{2.2}$$

2.1. Governing equations

The fundamental equations for dynamics can be found in Monaghan (2000). The equation of continuity is the following equation (2.3),

$$\dot{\rho} = \frac{d\rho}{dt} = -\rho \frac{\partial u^\alpha}{\partial \boldsymbol{q}^\alpha}, \tag{2.3}$$

where $\frac{d}{dt}$ represents the Lagrangian time derivative, u^α represents the α-th component of the velocity $\boldsymbol{u}$, and $\boldsymbol{q}^\alpha$ represents the α-component of the position $\boldsymbol{q}$.
The equation of the motion is given in the following equation (2.4),

$$\dot{u}^\alpha = \frac{1}{\rho} \frac{\partial \sigma^{\alpha\beta}}{\partial \boldsymbol{q}^\beta}, \tag{2.4}$$

With $\sigma^{\alpha\beta}$ is the stress tensor, where α, β are indices for reference axes in Cartesian coordinates. The equation of motion Eq. (2.4) has another expression,

$$\dot{u}^{\alpha} = -\frac{1}{\rho}\frac{\partial}{\partial \boldsymbol{q}^{\beta}}\left(\frac{\sigma^{\alpha\beta}}{\rho}\right) - \frac{\sigma^{\alpha\beta}}{\rho^2}\frac{\partial \rho}{\partial \boldsymbol{q}^{\beta}}. \tag{2.5}$$

In addition, the equation of energy is as follows:

$$\dot{e} = \frac{\sigma^{\alpha\beta}}{\rho}\dot{\varepsilon}^{\alpha\beta}, \tag{2.6}$$

where e is the specific internal energy, $\dot{\varepsilon}^{\alpha\beta}$ is the strain rate tensor, which can be expressed as follows Eq. (2.7),

$$\dot{\varepsilon}^{\alpha\beta} = \frac{1}{2}\left(\frac{\partial \nu^{\alpha}}{\partial \boldsymbol{q}^{\beta}} + \frac{\partial \nu^{\beta}}{\partial \boldsymbol{q}^{\alpha}}\right). \tag{2.7}$$

$\sigma^{\alpha\beta}$ being a symmetric tensor, Eq. (2.6) can be expressed by simpler form, as follows:

$$\dot{e} = -\frac{\sigma^{\alpha\beta}}{\rho}\frac{\partial \nu^{\alpha}}{\partial \boldsymbol{q}^{\beta}}. \tag{2.8}$$

As with the symmetric form relatively to the velocity, we write Eq. (2.8),

$$\dot{e} = \frac{1}{2}\left[\frac{\sigma^{\alpha\beta}}{\rho^2}\left(\nu^{\alpha}\frac{\partial \rho}{\partial \boldsymbol{q}^{\beta}} - \frac{\partial\left(\rho\nu^{\alpha}\right)}{\partial \boldsymbol{q}^{\beta}}\right) + \nu^{\alpha}\frac{\partial}{\partial \boldsymbol{q}^{\beta}}\left(\frac{\sigma^{\alpha\beta}}{\rho}\right) - \frac{\partial}{\partial \boldsymbol{q}^{\beta}}\left(\frac{\sigma^{\alpha\beta}\nu^{\alpha}}{\rho}\right)\right]. \tag{2.9}$$

2.2. Discretized governing equations and numerical corrections

Conservation Eqs.(2.3)-(2.6) can be discretized $\forall i \in \boldsymbol{K}$ to particle-approximation form as,

$$\dot{\rho}_i = \rho_i \sum_{j \in \boldsymbol{K_i}}\left[\frac{m_j}{\rho_j}\left(u_i - u_j\right) + \varepsilon h c_0 \Phi_{ij}\right] \cdot \nabla_i \widehat{W}_{ij}, \tag{2.10}$$

$$\dot{u}_i^{\alpha} = \sum_{j \in \boldsymbol{K_i}} m_j \left[\frac{\sigma_i^{\alpha\beta}}{\rho_i^2} + \frac{\sigma_j^{\alpha\beta}}{\rho_j^2} - \delta^{\alpha\beta}\Pi_{ij}\right] \nabla_i^{\beta}\widehat{W}_{ij}, \tag{2.11}$$

$$\dot{e}_i = \frac{1}{2}\sum_{j \in \boldsymbol{K_i}} m_j \left[\frac{\sigma_i^{\alpha\beta}}{\rho_i^2} + \frac{\sigma_j^{\alpha\beta}}{\rho_j^2} + \delta^{\alpha\beta}\Pi_{ij}\right]\left[u_i^{\beta} - u_j^{\beta}\right] \nabla_i^{\beta}\widehat{W}_{ij}, \tag{2.12}$$

where $\delta^{\alpha\beta}$ is Kronecker delta. A consistent form of kernel gradient (Chen et al., 1999) is used as,

$$\nabla_j \widehat{W}_{ij} = \boldsymbol{L}_i^{-1}\nabla_i W_{ij}, \tag{2.13}$$

where,

$$\boldsymbol{L}_i = -\sum_{j \in \boldsymbol{K_i}} \frac{m_j}{\rho_j}(\boldsymbol{q}_i - \boldsymbol{q}_j) \otimes \nabla_i W_{ij}, \tag{2.14}$$

with W_{ij} is the Wendland kernel as given below

$$W_{\boldsymbol{r}}(\|\boldsymbol{q}_{ij}\|_2, h) = \iota_d \begin{cases} \left(1 - \dfrac{\boldsymbol{r}}{2}\right)^4 (2\boldsymbol{r}+1) & \text{if} \quad 0 \leq \boldsymbol{r} < 2 \\ 0 & \text{otherwise} \end{cases}, \tag{2.15}$$

where, $\iota_d = \frac{21}{16\pi h^3}$ and $\boldsymbol{r} = \frac{\|\boldsymbol{q}_{ij}\|_2}{h}$. In the discrete momentum and energy equations, Π_{ij} is the artificial viscosity (Monaghan and Gingold, 1983). This is a corrective technic that can damp the numerical oscillations that can appear in a discontinuity area. The formulation is given by:

$$\Pi_{ij} = \begin{cases} \dfrac{-\kappa_1 h \bar{c}_{ij} \varphi_{ij} + \kappa_2 h^2 \varphi_{ij}^2}{\bar{\rho}_{ij}} & \text{if} \quad \boldsymbol{q}_{ij} \cdot \boldsymbol{u}_{ij} < 0 \\ 0 & \text{otherwise} \end{cases}, \tag{2.16}$$

with

$$\varphi_{ij} = \frac{\boldsymbol{q}_{ij} \cdot \boldsymbol{u}_{ij}}{\boldsymbol{q}_{ij}^2 + \epsilon h^2} \sim \nabla \cdot \boldsymbol{u}_i \sim \nabla \cdot \boldsymbol{u}_j. \tag{2.17}$$

In this formulation, the notation $\bar{c}_{ij}$, or $\bar{\rho}_{ij}$, corresponds to the average of quantity of two points i and j. The parameters c, κ_1, and κ_2 correspond, respectively, to the speed of sound in the material and two numerical parameters. These parameters may be determined through numerical experiments. In this framework, we adopt the δ-SPH scheme proposed by (Marrone et al., 2011) in which a proper artificial diffusive term Φ_{ij} is used into the continuity equation (2.10) to remove the spurious numerical high-frequency oscillations in the pressure field. Thus, Φ_{ij} can be expressed by simpler form as,

$$\Phi_{ij} = 2(\rho_i - \rho_j) \frac{\boldsymbol{q}_{ij}}{\|\boldsymbol{q}_{ij}\|_2^2} - (\dot{\rho}_i^* + \dot{\rho}_j^*), \tag{2.18}$$

where $\dot{\rho}^*$ is the renormalized density gradient (Randles and Libersky, 1996) defined as:

$$\dot{\rho}_i^* = -\sum_{j \in \boldsymbol{K_i}} \frac{m_j}{\rho_j} (\rho_i - \rho_j) \boldsymbol{L}_i^{-1} \nabla_i W_{ij}, \tag{2.19}$$

Coefficients ρ_0, c_0 and ε in Eq. (2.10) are, respectively, the initial density of material, the reference speed of sound and a parameter which controls the intensity of the diffusion of density.

3. Elastic-plastic SPH model

In the framework of HVI, the present paper proposes to investigate the perforation of thin metal plate by a projectile, using the original SPH approach. To model the different components (target and projectile), a hydrodynamic, elasto-plastic behaviour was considered and implemented in 3D code.

3.1. Constitutive model

The stress tensor was decomposed into two parts: the hydrostatic pressure P and a deviatoric part of the stress tensor $S^{\alpha\beta}$,

$$\sigma^{\alpha\beta} = -P\delta^{\alpha\beta} + S^{\alpha\beta}. \tag{3.1}$$

The pressure P proposed in this work was computed from the Mie Gruneisen equation of state, and was coupled to a constitutive law defining the deviatoric stress components of the stress tensor. Then, the following equations can be written:

$$P = (1 - \frac{1}{2}\Gamma_0\eta)P_h(\rho) + \Gamma_0 e, \tag{3.2}$$

$$P_h(\rho) = \begin{cases} \sum_{k=1}^{3} C_k\,\eta^k & \text{if } \eta \geq 0 \\ C_1\,\eta & \text{if } \eta < 0 \end{cases} \quad \text{with} \quad \eta = \frac{\rho}{\rho_0} - 1, \tag{3.3}$$

where Γ_0 represents the Gruneisen parameter linked to thermomechanical behavior. The pressure terms P_h was associated to the Hugoniot curve with the following C_k coefficient :

$$C_1 = \rho_0 c_0^2, \quad C_2 = C_1(1 + 2(s-1)), \quad C_3 = C_1(2(s-1) + 3(s-1)^2)\cdot \tag{3.4}$$

Four parameters $(\rho_0, s, c_0, \Gamma_0)$ were essential to defined this behavior law. The deviatoric stress component $S^{\alpha\beta}$ can be integrated through the incremental of Hooke's law with the Jaumann rate correction as,

$$\dot{S}_i^{\alpha\beta} = 2\mu(\dot{\varepsilon}_i^{\alpha\beta} - \frac{1}{3}\delta^{\alpha\beta}\dot{\varepsilon}_i^{\gamma\gamma}) + S_i^{\alpha\gamma}\dot{\omega}_i^{\beta\gamma} + S_i^{\gamma\beta}\dot{\omega}_i^{\alpha\gamma}, \tag{3.5}$$

where μ, $\dot{\varepsilon}^{\gamma\gamma}$ and $\dot{\omega}_i^{\alpha\gamma}$ were the shear modulus, the strain rate tensor and the rotation rate tensor, respectively. They were discretized into the SPH formulations as,

$$\dot{\varepsilon}_i^{\alpha\beta} = \frac{1}{2}\sum_{j\in \boldsymbol{K_i}} \frac{m_j}{\rho_j}\left[u_{ji}^{\alpha}\nabla_i^{\beta}\widehat{W}_{ij} + u_{ji}^{\beta}\nabla_i^{\alpha}\widehat{W}_{ij}\right], \tag{3.6}$$

$$\dot{\omega}_i^{\alpha\beta} = \frac{1}{2}\sum_{j\in \boldsymbol{K_i}} \frac{m_j}{\rho_j}\left[u_{ji}^{\alpha}\nabla_i^{\beta}\widehat{W}_{ij} - u_{ji}^{\beta}\nabla_i^{\alpha}\widehat{W}_{ij}\right]\cdot \tag{3.7}$$

The plastic behavior was based on the Von Mises Yield criterion by using a pressure independent yield function

$$\mathrm{y}_f = \sqrt{J_2} - \frac{\sigma_\mathrm{y}}{\sqrt{3}}, \tag{3.8}$$

where $J_2 = \frac{1}{2}S^{\alpha\beta}S^{\alpha\beta}$ represents the second stress tensor invariant, and σ_y represents the Yield stress. The plastic behaviour is reached if the stress yield criterion is met ($(\mathrm{y}_f > 0)$. The criteria may be used to bring back the deviatoric stress component to the Yield surface as

$$S_{\text{new}}^{\alpha\beta} = c_\mathrm{y} S_{\text{old}}^{\alpha\beta}, \tag{3.9}$$

where $c_\mathrm{y} = \min(1, \frac{\sigma_\mathrm{y}}{\sqrt{3J_2}})$. The definition of the plastic strain increment, effective plastic strain increment can be written, respectively, as,

$$\Delta\varepsilon_{\text{pl}}^{\alpha\beta} = \frac{1 - c_\mathrm{y}}{2\mu} S^{\alpha\beta}, \tag{3.10}$$

$$\Delta\varepsilon_{\text{pl}} = \frac{1 - c_\mathrm{y}}{3\mu}\sqrt{\frac{3}{2}S^{\alpha\beta}S^{\alpha\beta}}. \tag{3.11}$$

These equations assumed that the plastic strain increment was in proportion to deviatoric stress for an elasto-plastic material.

3.2. Plasticity model

The Johnson and Cook (1983) elastic-plastic model which takes into account linear thermo-elasticity, the Von Mises Yield criterion, plastic flow, strain-rate hardening, strain hardening, and thermal softening of the material was used as based model. The yield stress was given by equation (3.12):

$$\sigma_{\mathrm{y}} = \left[A + B\left(\varepsilon_{\mathrm{pl}}^{\mathrm{eff}}\right)^{N}\right]\left[1 + C\ln\left(\frac{\dot{\varepsilon}_{\mathrm{pl}}^{\mathrm{eff}}}{\dot{\varepsilon}_{0}}\right)\right]\left[1 - (T_{\mathrm{n}})^{M}\right], \tag{3.12}$$

where A, B, C, N and M were material constants. $\varepsilon_{\mathrm{pl}}^{\mathrm{eff}}$, $\dot{\varepsilon}_{\mathrm{pl}}^{\mathrm{eff}}$ and $\dot{\varepsilon}_0$ were, respectively, the accumulated effective plastic strain, the rate of plastic strain rate and the reference value of plastic strain rate. T_{n} was the normalized temperature given by equation (3.13):

$$T_{\mathrm{n}} = \left(\frac{T - T_{\mathrm{tr}}}{T_{\mathrm{m}} - T_{\mathrm{tr}}}\right), \tag{3.13}$$

where T, T_{m}, T_{tr} were, respectively, the current temperature, the melting temperature and the transition temperature. Analytically speaking and without taking into account the external heat sources and convection effects, the temperature evolution can be expressed as given in the following formula,

$$\dot{T} = \frac{1}{\rho C_{\mathrm{p}}}\dot{\varepsilon}_{\mathrm{pl}}^{\alpha\beta} S^{\alpha\beta}, \tag{3.14}$$

where C_{p} was the specific heat of concerned material.

4. Contact and failure algorithm

4.1. Management of the contact

The management of the contact is a poorly explored field in the framework of particle methods. The problem of contact can be written in the form of a minimization problem under constraints. Two methods are frequently used: the Lagrange multipliers method and the penalty method. The penalty method is a simple method that is used to add a penalty when the solution of the problem violates the constraint. To introduce the management of the contact in the developed code, we propose to use a penalty method as performed in (Belytschko and Yeh, 1993; Campbell et al., 2000; Vignjevic and Campbell, 1999). This technic allowed us to introduce the contact between SPH body without requiring a costly procedure in terms of time computation. Contact treatment of contact detection and contact force applications was considered using particle to particle contact. In this case, a contact occurred when the intersection of two compact supports of two particles i and k from two different bodies $\boldsymbol{B_i^1}$ and $\boldsymbol{B_k^2}$, respectively, was not empty ($\boldsymbol{\Omega}_{\boldsymbol{B_i^1}} \cap \boldsymbol{\Omega}_{\boldsymbol{B_k^2}} \neq \emptyset$) as shown in Fig. 1. Then, the penetration was determined by the following equation (4.1):

$$\mathfrak{p}_{ik} = h_i + h_k - \|\boldsymbol{q}_{ik}\|_2, \tag{4.1}$$

The penalty force was exerted in the direction between particles. To apply the penalty force, the normal vector at each boundary particle was found as

$$\mathfrak{n}_{ik} = \frac{\boldsymbol{q}_{ik}}{\|\boldsymbol{q}_{ik}\|_2}, \tag{4.2}$$

Concerning the choice of the penalty force $\mathfrak{F}^{\mathfrak{p}}$ (Belytschko and Yeh, 1993; Vignjevic and Campbell, 1999) to be affected in the case of penetration ($\mathfrak{p}_{ik} \geq 0$), which was defined as follows:

$$\mathfrak{F}^{\mathfrak{p}}_{ik} = K_{\mathfrak{p}} \max\left(\mathfrak{F}^{1}_{ik}, \mathfrak{F}^{2}_{ik}, \mathfrak{F}^{3}_{ik}\right) \mathfrak{n}_{ij}, \tag{4.3}$$

where $K_{\mathfrak{p}}$ was a scale factor. The forces $\mathfrak{F}^{1}_{ik}$, $\mathfrak{F}^{2}_{ik}$, and $\mathfrak{F}^{3}_{ik}$ were, respectively:

$$\mathfrak{F}^{1}_{ik} = \frac{m_k}{m_i} \frac{\mathfrak{p}_{ik}}{\Delta t^2}, \tag{4.4}$$

$$\mathfrak{F}^{2}_{ik} = \sqrt{\frac{h_i h_k}{h_i + h_k}} \left(\frac{\mu_i \mu_k}{\mu_i + \mu_k}\right) \frac{\mathfrak{p}_{ik}^{\frac{3}{2}}}{m_i}, \tag{4.5}$$

$$\mathfrak{F}^{3}_{ik} = \frac{1}{m_i} \left(\frac{\rho_i \rho_k h_i^3 h_k^3}{\rho_i h_i^3 + \rho_k h_k^3}\right) \frac{\dot{\mathfrak{p}}_{ik}}{\Delta t} \quad \text{if} \quad \dot{\mathfrak{p}}_{ik} > 0, \tag{4.6}$$

where Δt is the time step and $\dot{\mathfrak{p}}_{ik}$ is the rate of penetration.

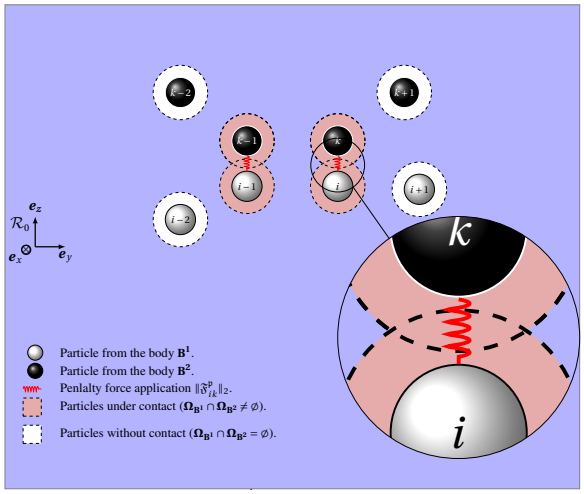

Fig 1: Management of the contact: diagram of the penetration area.

4.2. Failure algorithm

The fracture behavior implemented in the model was based on the Johnson and Cook (1985) dynamic failure model. The model that takes into account the stress triaxiality ratio, strain rate and temperature is given by equation (4.7):

$$\varepsilon_f^{pl} = \left[D_1 + D_2 \exp\left(D_3 \frac{\sigma_{\mathrm{m}}}{\sigma_{\mathrm{eq}}}\right)\right] \left[1 + D_4 \ln\left(\frac{\dot{\varepsilon}_{\mathrm{pl}}^{\mathrm{eff}}}{\dot{\varepsilon}_0}\right)\right] \left[1 + D_5 T_{\mathrm{n}}\right], \tag{4.7}$$

where $D_1 \sim D_5$ are material constants, $\frac{\sigma_{\mathrm{m}}}{\sigma_{\mathrm{eq}}}$ is defined as the ratio of the mean stress σ_{m} to the Von Mises equivalent σ_{eq}. Once initiated, the damage in the material was assumed to evolve linearly until the material was degraded. The damage, $\mathfrak{D}$, accumulated in a particle is given by:

$$\mathfrak{D} = \sum \frac{\Delta \varepsilon_{\mathrm{pl}}}{\varepsilon_f^{pl}}, \tag{4.8}$$

Failure occurs when $D \geq 1$. Once this condition was satisfied, a particle was removed from the simulation. This damage model was required in the finite element method involving HVI problems that lead to distortion of the element, even though the distortion of the particles would not happen in this model. In the present study, the damage model was assumed to occur when accumulated plastic strain $\varepsilon_{\mathrm{pl}}$ reached a critical value $\varepsilon_{\mathrm{pl}}^c$. Thus, the real time damage $\mathfrak{D}$ is calculated-through the condition

$$\mathfrak{D} = \begin{cases} 1 & \text{if} \quad \varepsilon_{\mathrm{pl}} \geq \varepsilon_{\mathrm{pl}}^c \\ \\ 0 & \text{otherwise} \end{cases}, \tag{4.9}$$

leading to $D_2 = D_4 = D_5 = 0$ in Eq. (4.7). The damage model introduced a new philosophy to interpret the interactions between particles which takes several different cases: undamaged with partial damaged, undamaged with fully damaged particle and partial damaged with fully damaged. To reduce the interactions, the value of the kernel function and the gradient of kernel function were replaced when the damage appears for each particle, as shown in Fig. 2. The interactions were controlled with a modified kernel function (4.10), which depends on the damage value

$$\overline{W}_{ij} = (1 - \mathfrak{D}_{ij}) \widehat{W}_{ij}, \tag{4.10}$$

$\mathfrak{D}_{ij}$ was defined as $\mathfrak{D}_{ij} = \frac{1}{2}(\mathfrak{D}_i + \mathfrak{D}_j)$, where $\mathfrak{D}_i$ and $\mathfrak{D}_j$ were the damage value in ith and jth particles, respectively.

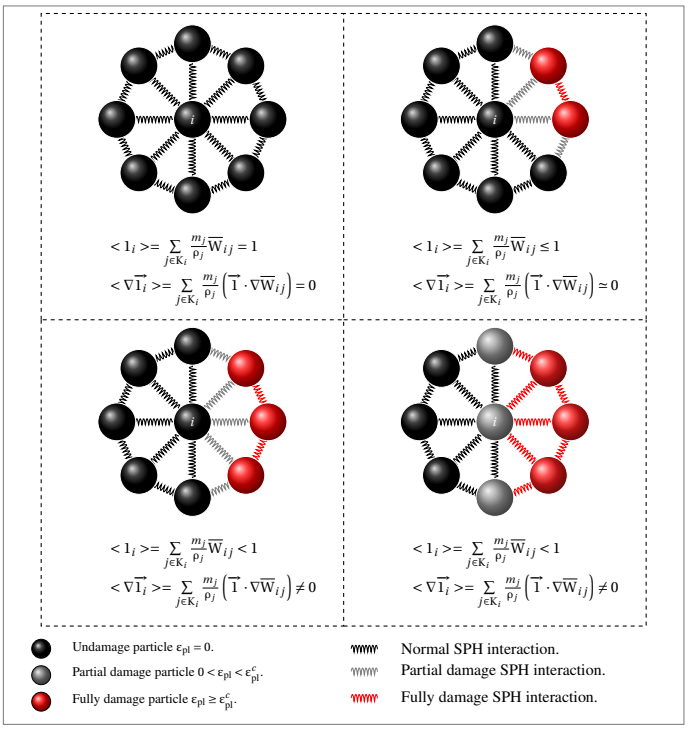

Fig 2: Crack propagation through damaged kernels.

Several performance issues were found during the implementation of the SPH system and the impact simulation. The most important was the time computations, which prevented any interactivity for the simulations of just a few hundred particles. This performance problem could be improved algorithmically and the solution is described in the following section.

5. Implementation and integration scheme on GPU

5.1. GPU implementation

The evaluation of SPH terms iterated through all particles. Because each particle must evaluate several SPH terms, the naive time complexity for the simulation with N particles was bounded by $O(N^2)$. An asymptotic squared running time complexity was not satisfactory and deviated from any interactive speed as the amount the particles grow. The smoothing kernels all had the finite compact support radius $2h$, and by definition the kernel contribution from any particle located beyond $2h$ was zero. A cell-linked list searching approach (Domìnguez et al., 2011) was therefore implemented to reduce the size of the search domain for the SPH body and thus accelerated the neighbor searching process. A simple 2D view of the cell-linked list searching approach applied to particles of the same body where their support had the same size $2h$ is shown in Fig. 3. This approach was implemented using C++ and CUDA (Compute Unified Device Architecture), which was developed by NVIDIA. This GPU program was formulated using a SPMD (single-program multiple data) technique, where the same program is simultaneously executed by blocks of threads. From the discrete formulation of the SPH, the threads are assigned to each particle. The GPU kernel functions allowed us to do all of the calculations (neighbor searching, internal forces, contact algorithm, etc.) independently for each particle.

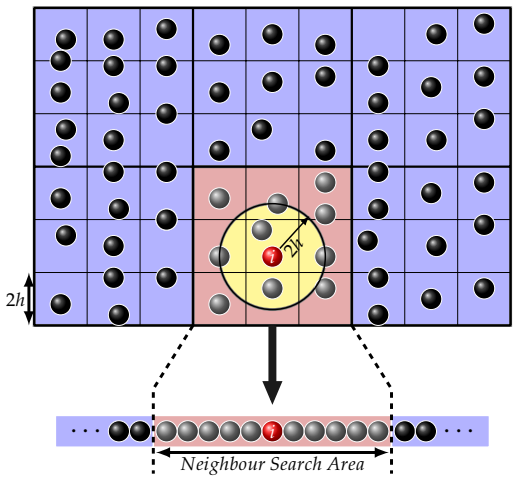

Fig 3: The cell-linked list using cells of size 2hx2h.

As illustrated in Fig. 4, the current GPU code model was divided into five components that were related to initial configuration, neighbor searching, particle interaction, contact algorithm and time integration. The initial configuration was designed to set the initial filed values (the positions, velocities of particles and physical parameters values) in the beginning of simulation, into the host (CPU memory) and to copy them on the device (GPU memory). Neighbor searching was one of the most important steps of the SPH algorithm. The neighbors of each particles were identified and stored on a neighbor list. After the creation of the neighbor list, the SPH calculation could start.

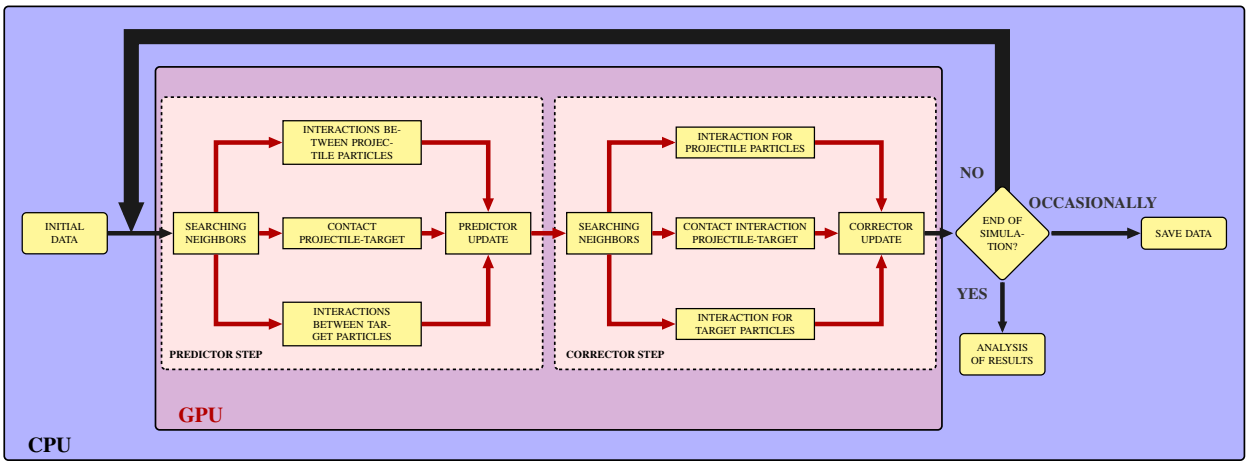

Fig 4: Algorithm for the impact 3D-GPU code.

The pressure of particles was updated using the equation of state Eq. (3.2). Then, the interaction between particles from the same body was calculated by solving the continuity and momentum equations Eqs. (2.11)-(2.10). The force contact on the different body particles was calculated using a Projectile-Target contact definition in Eq-(4.3). These calculations were repeated over the simulation time. It should be noted that the current GPU model was entirely executed on the device by means of issuing a set of CUDA kernel

functions, which avoided the time-consuming communication between the host and device.

5.2. Time integration scheme

The density, velocity, position and plasticity damage of each SPH body were updated by using the explicit integration method predictor-corrector scheme as illustrated in Fig. 5. A CFL condition was used to determine the variable time step size Δt as

$$\Delta t = C_{\text{CFL}} \min_i \left(\frac{h_i}{c_0 + \max_k |u_k|} \right), \tag{5.1}$$

where C_{CFL} is CFL coefficient.

input : Particles position, initial variables value and material parameters

STEP 1 : **Predictor**

for ***all*** *particle* i **do**
  find neighbors j
end
for ***all*** *particle* i **do**
  compute $[\dot{\rho}_i]^{n+\frac{1}{2}}$, $[\dot{\varepsilon}_i^{\alpha\beta}]^{n+\frac{1}{2}}$, $[\dot{\omega}_i^{\alpha\beta}]^{n+\frac{1}{2}}$, $[\dot{S}_i^{\alpha\beta}]^{n+\frac{1}{2}}$, $[P_i]^{n+\frac{1}{2}}$, $[\sigma_i^{\alpha\beta}]^{n+\frac{1}{2}}$ and $[\dot{u}_i]^{n+\frac{1}{2}}$
  compute $[\mathfrak{f}_i^{\mathfrak{p}}]^{n+\frac{1}{2}} = \sum_{k\in \boldsymbol{K_i}} \mathfrak{F}_{ik}^{\mathfrak{p}}$ and σ_{y}
end
for ***all*** *particle* i **do**
  $[q_i]^{n+\frac{1}{2}} = [q_i]^n + (\Delta t)[u_i]^{n+\frac{1}{2}} + (\Delta t)^2([\dot{u}_i]^{n+\frac{1}{2}} + [\mathfrak{f}_i^{\mathfrak{p}}]^{n+\frac{1}{2}})$
  $[u_i]^{n+\frac{1}{2}} = [u_i]^n + (\Delta t)([\dot{u}_i]^{n+\frac{1}{2}} + [\mathfrak{f}_i^{\mathfrak{p}}]^{n+\frac{1}{2}})$
  $[\rho_i]^{n+\frac{1}{2}} = [\rho_i]^n + (\Delta t)[\dot{\rho}_i]^{n+\frac{1}{2}}$
  $[S_i^{\alpha\beta}]^{n+\frac{1}{2}} = [S_i^{\alpha\beta}]^n + (\Delta t)[\dot{S}_i^{\alpha\beta}]^{n+\frac{1}{2}}$
  $\mathrm{y}_f = \sqrt{J_2} - \frac{\sigma_{\mathrm{y}}}{\sqrt{3}}$
  if $y_f > 0$ **then**
    $[S_{i,\mathrm{New}}^{\alpha\beta}]^{n+\frac{1}{2}} = c_{\mathrm{y}}[S_i^{\alpha\beta}]^{n+\frac{1}{2}}$
  end
  compute $[\Delta\varepsilon_{i,\mathrm{pl}}^{\alpha\beta}]^{n+\frac{1}{2}} = \dfrac{1-c_{\mathrm{y}}}{2\mu}[S_i^{\alpha\beta}]^{n+\frac{1}{2}}$
  $[\varepsilon_{i,\mathrm{pl}}^{\alpha\beta}]^{n+\frac{1}{2}} = [\varepsilon_{i,\mathrm{pl}}^{\alpha\beta}]^n + [\Delta\varepsilon_{i,\mathrm{pl}}^{\alpha\beta}]^{n+\frac{1}{2}}$
  compute $\varepsilon_{i,\mathrm{pl}}$
  if $\varepsilon_{i,pl} > \varepsilon_{i,pl}^c$ **then**
    $\mathfrak{D}_i = 1$
  else
    $\mathfrak{D}_i = 0$
  end
end

STEP 2 : **Corrector**

for ***all*** *particle* i **do**
  find neighbors j
end
for ***all*** *particle* i **do**
  compute $[\dot{\rho}_i]^{n+1}$, $[\dot{\varepsilon}_i^{\alpha\beta}]^{n+1}$, $[\dot{\omega}_i^{\alpha\beta}]^{n+1}$, $[\dot{S}_i^{\alpha\beta}]^{n+1}$, $[P_i^{n+1}]$, $[\sigma_i^{\alpha\beta}]^{n+1}$ and $[\dot{u}_i]^{n+1}$
  compute $[\mathfrak{f}_i^{\mathfrak{p}}]^{n+1}$ and σ_{y}
end
for ***all*** *particle* i **do**
  $[u_i]^{n+1} = [u_i]^{n+\frac{1}{2}} + (\frac{\Delta t}{2})([\dot{u}_i]^{n+1} - [\dot{u}_i]^{n+\frac{1}{2}} + [\mathfrak{f}_i^{\mathfrak{p}}]^{n+1})$
  $[\rho_i]^{n+1} = [\rho_i]^{n+\frac{1}{2}} + (\frac{\Delta t}{2})([\dot{\rho}_i]^{n+1} - [\dot{\rho}_i]^{n+\frac{1}{2}})$
  $[S_i^{\alpha\beta}]^{n+1} = [S_i^{\alpha\beta}]^{n+\frac{1}{2}} + (\frac{\Delta t}{2})([\dot{S}_i^{\alpha\beta}]^{n+1} - [\dot{S}_i^{\alpha\beta}]^{n+\frac{1}{2}})$
  $\mathrm{y}_f = \sqrt{J_2} - \frac{\sigma_{\mathrm{y}}}{\sqrt{3}}$
  if $y_f > 0$ **then**
    $[S_{i,\mathrm{New}}^{\alpha\beta}]^{n+1} = c_{\mathrm{y}}[S_i^{\alpha\beta}]^{n+1}$
  end
  compute $[\Delta\varepsilon_{i,\mathrm{pl}}^{\alpha\beta}]^{n+1} = \dfrac{1-c_{\mathrm{y}}}{2\mu}[S_i^{\alpha\beta}]^{n+1}$
  $[\varepsilon_{i,\mathrm{pl}}^{\alpha\beta}]^{n+1} = [\varepsilon_{i,\mathrm{pl}}^{\alpha\beta}]^{n+\frac{1}{2}} + [\Delta\varepsilon_{i,\mathrm{pl}}^{\alpha\beta}]^{n+1}$
  compute $\varepsilon_{i,\mathrm{pl}}$
  if $\varepsilon_{i,pl} > \varepsilon_{i,pl}^c$ **then**
    $\mathfrak{D}_i = 1$
  else
    $\mathfrak{D}_i = 0$
  end
end

Fig 5: The HVI-SPH GPU algorithm adapted to the plasticity damage and fracture by using predictor-corrector scheme.

In the simulations, the initial particle spacing was limited $\Delta q \in [0.1, 1.0]$ mm and approximately between two and eight million particles were used for the projectile and the target. Note that simulations of cylindrical projectile impacting on thick target required more computational efforts (numerical parameters, particle spacing, etc.). These parameters were taken from a numerical convergence study and they are listed in the next section.

6. Numerical simulations

To validate the numerical model, we conducted an experimental work on a Weldox 460 E steel target with two thickness (T_t) and different impact velocities (Børvik et al., 2001b, 2003). The impact velocities

varied for both target thickness from 137.4 to 298 m/s for a target plate of 8mm thickness and 177.3 to 399.6 m/s for a 12mm thickness. The different experimental cases are listed in Table 1.

Scenario	Speed of impact (m/s)	Target thickness (mm)
1	298	8
2	250.8	8
3	190.7	8
4	165.2	8
5	160	8
6	156	8
7	152.5	8
8	137.4	8
9	399.6	12
10	303.5	12
11	285.4	12
12	224.7	12
13	200.4	12
14	189.6	12
15	181.5	12
16	177.3	12

Table 1: Table of scenarios impact on an 8 mm and 12 mm thick plate, reproduced from (Børvik et al., 2003).

The 3D representation of the initial geometry of both targeted plate geometry and projectile is illustrated in Fig. 6. The target had a radius (R_T) of 250 mm. The projectile length (L_P), radius (R_P) and mass (m_P) were kept constant in the tests and were 80 mm, 10 mm and 197 g respectively. The developed 3D SPH model was used to study the effect of impact velocities and targeted plate thickness on the velocity of the plug and also of the projectile after the impact. Initial velocity of the projectile was considered as initial conditions, whereas null velocity and stress were considered in the targeted plate. Boundary conditions consisted in fixing a zero displacement and rotation at the cylinder periphery. The interaction between the projectile and the target was applied by using the particle contact algorithm.

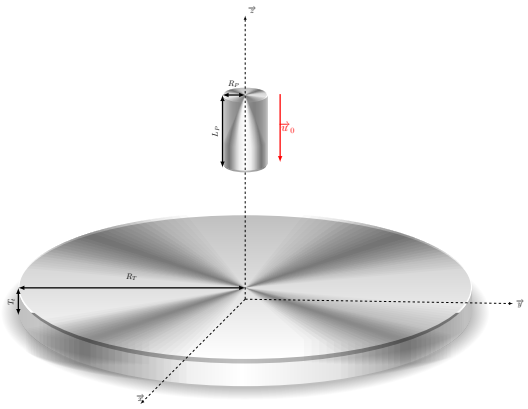

Fig 6: Initial representation of the impact. T_t and u_0 denote the Thickness of the target and the initial velocity vector respectively.

To be able to describe the various phenomena occurring during ballistic penetration, the SPH code developed for high velocity was used and the numerical results are compared to the experimental data proposed by (Børvik et al., 2001a, 2002). The target material was modeled as elastic-visco-plastic domain using the constitutive model that was developed by Johnson-Cook, the ductile damage for penetration problem, by assuming isotropic material behavior, Von Mises plasticity, and neglected thermal effects (Børvik et al., 2001a, 2002). The projectile with hardened tool steel was modeled as a linear elastic material. The parameters for Arne tool steel projectile and Weldox 460 E steel target are given in Table 2.

Property	**Target**	**Projectile**
Material	**Weldox 460 E**	**Arne tool steel**
Density ρ_0(km/m^3)	7850	7850
Modulus of Elasticity		
E (GPa)	200	205
Poisson's ratio ν	0.33	0.33
Johnson-Cook constitutive model parameters		
A (Mpa)	490	1900
B (Mpa)	807	0
C	0.0114	0
n	0.73	-
$\varepsilon_{\text{pl}}^{c}$	0.3	0.5
The Mie-Grüneisen Equation		
s	1.5	1.5
Γ_0	2	2
c_0 (m/s)	5047.60	5110.25

Table 2: Material properties of target plates and penetrator used in the numerical model (Børvik et al., 2002) and (Børvik et al., 2001a).

During the impact process, the dynamic failure $\mathfrak{D}$ took the value 1 when the variable ε_{pl} was greater than

$\varepsilon^c_{\text{pl}}$. The variable $\mathfrak{D}$ was calculated during every single integration cycle according to the algorithm in Fig. 5. As recommended in Ren and Li (2010), the critical plastic shear strain coefficient is considered to be small in impact problems.
The particle number was directly related to particle spacing and consequently affects the computing efficiency if the number was too important. Therefore, a sensitivity study was conducted to investigate the reliance of the results on the particle spacing $\Delta \boldsymbol{q}$. Other relevant numerical data are given in Table 3.

Artificial viscosity	Intensity of the diffusion	Contact scale factor	CFL coefficient
$(\kappa_1\ ,\ \kappa_2)$	ε	K_{p}	C_{CFL}
(1.0,1.0)	0.1	0.3	0.05

Table 3: Numerical parameters used for plugging failure.

The simulation runs were carried out until the duration the projectile leaves the both target plate with constant residual velocity. This practice was followed for both target plate thickness and for all impact velocities.

7. Results and discussion

The SPH method was introduced to treat complex problems involving blunt projectile impacting thin plates in three dimension. This method is able to treat these kind of complex problems due to its meshless aspect. This numerical method does not require a grid to evaluate spatial derivatives, which allows a purely Lagrangian formulation to be used, even if important geometrical deformations appear. Thus, this method appears to be an interesting choice to handle penetrating impact problems where important deformations and failures occur. High speed impact phenomena on both thick target plates were studied through the proposed 3D-SPH GPU simulation method and the obtained results are discussed along with the corresponding available experimental results. The first target plate has a thickness of 8mm, which represents the impact scenarios from 1 to 8 in Table 1. The simulation runs were carried out from higher velocity value to lower velocity value, until the ballistic limit velocity, which corresponded to a 0 m/s residual velocity. The Fig. 7 shows the snapshots of the penetration history of the projectile during the impact. The cylinder penetrated and cut out the target during the impact. The simulation started from the projectile approaching the target at initial velocity 190.7 m/s. The interaction between the projectile and the target started when the contact was detected. At the initial part of impact (0-42μs), the plasticity split started to grow to generate a complete crack (187-210μs) toward the opposite side of the impact. Very high localized effective plastic strain was observed at the location of penetration. There was very little accumulation of plasticity outside this zone. After 210μs simulation time, the damage pattern in the target remained unchanged.

(a) Time = 11 μs.

(b) Time = 82 μs.

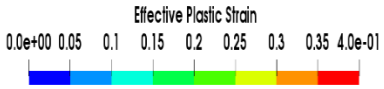

(c) Time = 187 μs.

(d) time = 210 μs.

Fig 7: Impact of a 20 mm diameter, 197 g Arne tool steel cylinder into a 8 mm thick Weldox 460 E plate. The impact velocity was 190.7 m/s (scenario 3).

The simulation results and corresponding experimental results for residual velocity of the plug and the projectile as a function of the initial velocity for 8 mm thickness of the target are illustrated in Fig. 8. It can be noted that there is a good correlation between experimental data and numerical results in terms of residual velocity. In addition, the velocity limit of perforation of the target was observed and the numerical simulation provided realistic results concerning this parameter. The ballistic limit velocity was found to be of 152.5 m/s, which was exactly the value obtained during experiments. Beyond this limit, residual velocity drastically increased with the initial velocity for both plug and projectile, which accurately correlated the experimental data.

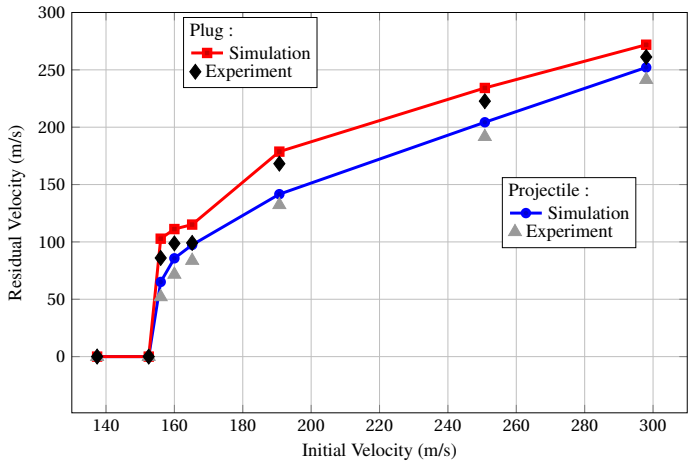

Fig 8: Residual velocities vs Impact velocities for projectile and plug for 8 mm thick Weldox 460 E steel plate.

As for 8 mm thickness, scenario 9 to 16 for 12 mm thickness were simulated, and results are provided in Fig. 9, where simulations and corresponding experimental results for residual velocity versus initial velocity curves are illustrated. It was observed that the trend of residual velocity obtained from numerical simulations were in good agreement with the experimental data.

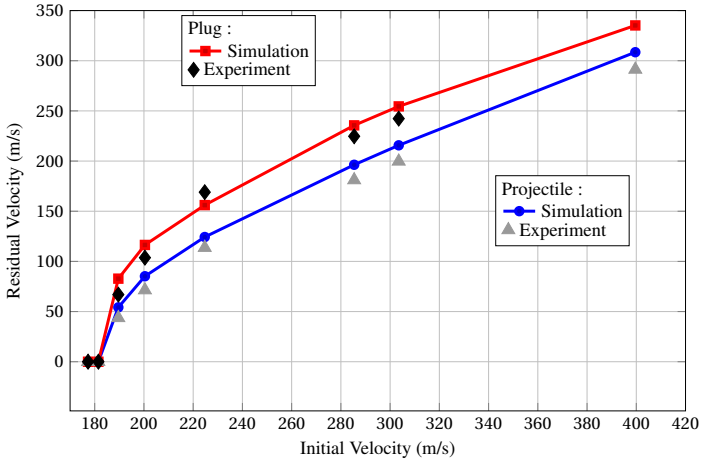

Fig 9: Residual velocities vs Impact velocities for projectile and plug for 12 mm thick Weldox 460 E steel plate.

The snapshots of the penetration history of the projectile during the impact, with the evolution of the failure, for scenario 9 is provided on Fig. 10. For this scenario, the failure propagation produced by an impact of projectile of 20 mm diameter, with an impact velocity of 399.6 m/s into target plate thickness of 12 mm. The high value of the effective plastic strain illustrates the failure propagation deduced by the penetration of the projectile.

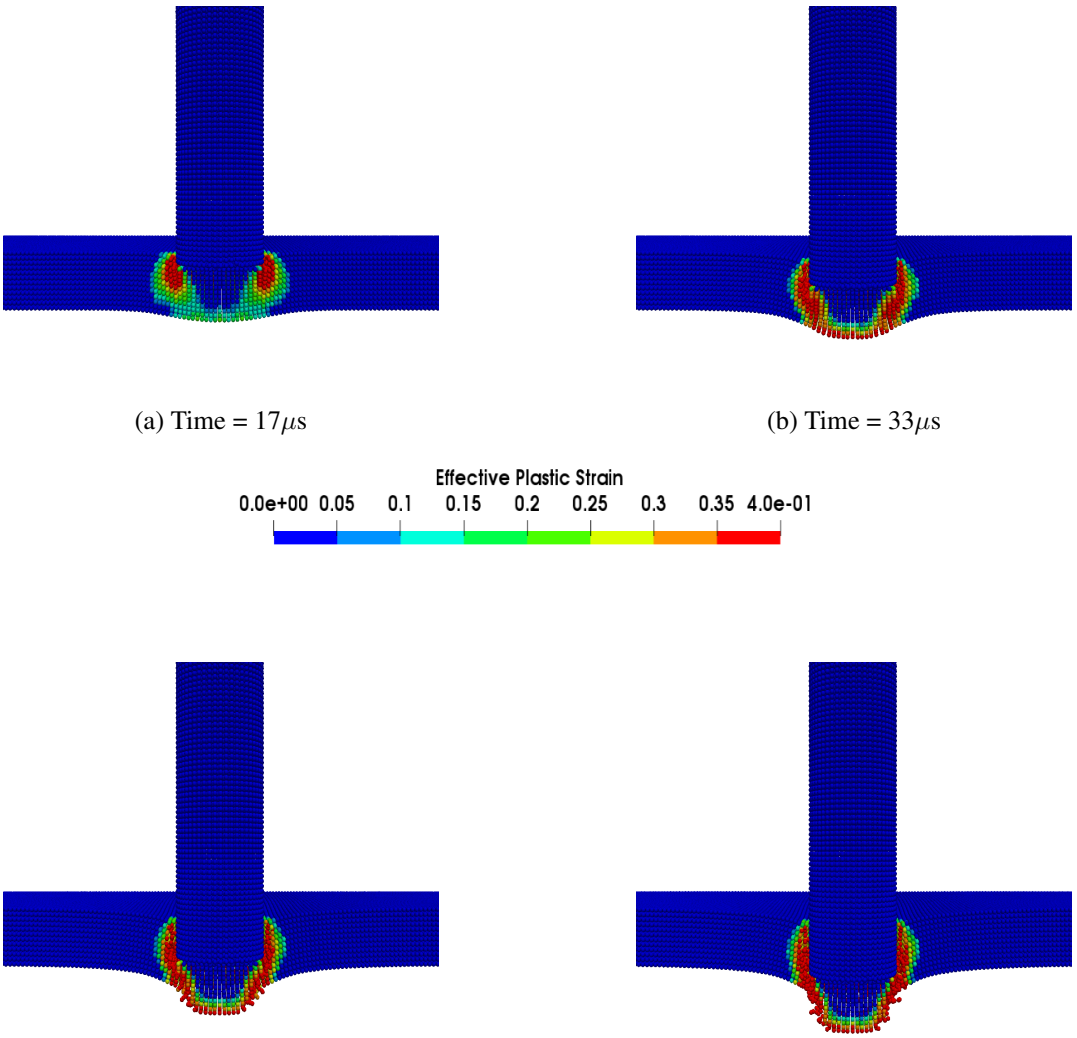

(a) Time = 17μs (b) Time = 33μs

(c) Time = 67μs (d) Time = 102μs

Fig 10: Shows a view of failure propagation produced by an impact of a 20 mm diameter, 197 g Arne tool steel cylinder into a 12 mm thick Weldox 460 E plate. The impact velocity was 399.6 m/s (scenario 9).

In the ballistic simulations presented in this study, the hydrodynamic aspect was coupled to the Johnson-cook viscoplastic behavior law and a simplified damage model was well adapted to HVI problems involving a thin steel target. Fig. 8 and Fig. 9 clearly show a typical comparison of experimental and numerical results. It can be observed that predicted results are in good correlation with the experimental results for all scenarios. The numerical simulations were also able to predict the ballistic limit with a very good accuracy. As shown in Fig. 7, there was no significance deformation of the projectile's diameter. This happened

because the yield strength for the projectiles is relatively higher than the yield strength of the target plate. The deformation of the target plate is highly localized. The target plates failed by removing a circular plug when impacted normally by blunt projectiles. It was observed from all cases that the diameter of the plug ejected from the target plate was approximately equal to the diameter of the projectile, which corresponds to the experimental observations. The plug stayed attached to the projectile during the perforation process and was eventually separated from the projectile, as can be seen at the end of Fig. 7.

The contact interface is defined in the algorithm, which was developed in the work of Belytschko and Yeh (1993) and adapted in Vignjevic and Campbell (1999) for SPH simulation. It consists of a penalty formulation, which involves repulsive forces between particles of projectile and particles of the target (particle to particle contact form). To reduce the instability of this numerical entity, corrective approaches have been implemented such as artificial viscosity and XSPH allowing non inter-penetration of particles and in reducing the numerical oscillations (artificial viscosity), and averaging of the velocity of particles (XSPH). Both of these corrective approaches can naturally lead to an important energy dissipation if the linear and quadratic coefficients of artificial viscosity and also the coefficient of velocity averaging are too high. A sensitivity study was conducted on these coefficients which concluded to correct reference values of these parameters, to avoid too important energy dissipation as in (Taddei et al., 2015). Fidelic residual velocity of the projectile and the plug as illustrated in different Fig. 8-9 highlight this point. In opening, the work of Shaw and Reid (2009); Shaw et al. (2011) can be cited. These authors worked on the control of the artificial viscosity coefficients, which could change during a simulation, by using heuristic correction and optimized form of acceleration.

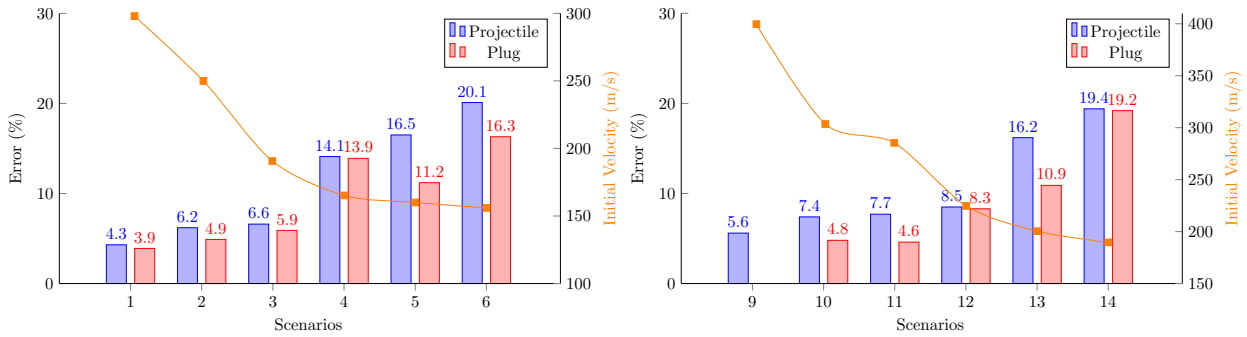

(a) 8 mm thick plate.

(b) 12 mm thick plate.

Fig 11: Relative error between Børvik's experimental cases and GPU-SPH simulation for the penetrating cases.

An analysis of the prediction of the simulated residual velocity, for both plug and projectile, on the penetrating impact cases provided the relative error between the experimental data and the numerical results in Fig. 11, which illustrates that the maximum error reached 20.1% for the scenarios corresponding to the lowest impact velocity. Indeed, difficulties can occur due to the choice of damage model and associated parameters, which can influence the strain localization. These phenomena should be taken into account to extend the validity domain of the model.

Like the classical numerical method, SPH is also sensitive to the space discretization and particle density. To investigate this important issue, a sensitivity study was carried out to study the effect of the spatial resolution process, as illustrated in Table 4. For three different spatial discretization (0.8,1.0, and 1.2 mm) and for four different cases, some previously described impact cases were simulated. Then, for the eight

added simulations (cases 1, 6, 10, 14, and two sets of discretization), increasing the particle density did not bring significant improvement in terms of errors when compared to reference simulations (1.0mm), whereas decreasing the particle density increased significantly the errors. Therefore, it can be concluded that the reference discretization (1mm) was a good compromise between accuracy and time computation.

Particle Spacing (mm)	Case	Physical time (μs)	Particle number	Total GPU time (s)	Computational steps	Residual error Projectile	Plug
0.8	1	310	3,424,425	34,560	25,600	4.1%	4.2%
	6	380		42,795	31,700	19.7%	16.1%
	10	300	4,958,310	36,250	25,000	4.4%	4.2%
	14	415		50,170	34,600	19.1%	18.9%
1.0	1	310	1,595,905	24643	20,500	4.3%	3.9%
	6	380		30,678	25,500	20.1%	16.3%
	10	300	3,241,792	27,125	20,000	7.4%	4.8%
	14	415		37,395	27,700	19.4%	19.2%
1.2	1	310	969,471	15,570	17,300	7.4%	6.8%
	6	380		19,083	21,200	24.3%	22.6%
	10	300	1,378,518	16,366	16,700	10.2%	7.9%
	14	415		12,838	23,100	23.3%	22.9%

Table 4: Results of the GPU simulations. For the cases 1, 6, 10 and 14. Results with the finest resolution are listed.

To demonstrate the benefits of using a GPU to accelerate these simulations, Fig. 12 shows the comparison of the results of the GPU to CPU computation using MPI (Frissane et al. (2018)). An important time speed was earned by the GPU algorithm in the range of 5–6 compared to a CPU algorithm. This comparison clearly shows the advantages of the massive parallelization provided by the GPU and parallel code. Fig. 13 shows the percentage of the total computational time for each GPU tasks: the neighbor searching, the particles interactions and the system integration. The interactions of the particles required the most computation time as already explained by (Mokos et al., 2015). This was the case for low distribution of particles, and its importance increased with the number of particles.

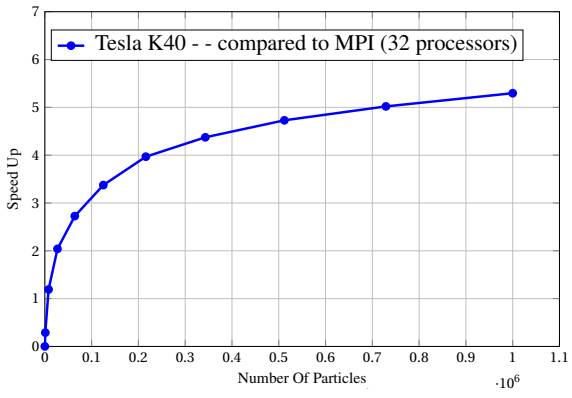

Fig 12: Runtime comparison between a CPU and GPU for a three dimensional case.

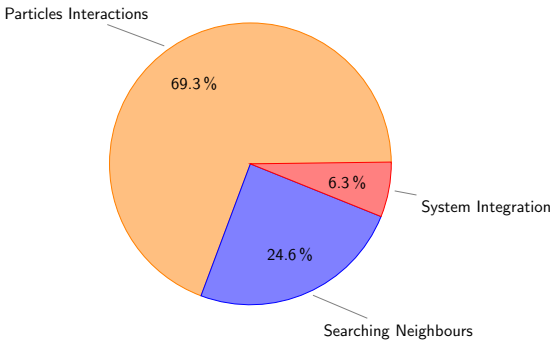

Fig 13: Percentage of the runtime taken by each part of the code for the Tesla-K40 card (1 million particles).

8. Conclusion

The problem of the perforation of thin steel plates by a blunt projectile was considered. Weldox 460 E steel plates of 8 mm and 12 mm thickness were normally impacted at various velocities by blunt projectiles. It was found that smoothed particle hydrodynamics implemented in GPU code with the Johnson-Cook material model and a simple damage model was capable of accurately predicting the perforation process. The results show that the developed SPH GPU numerical code was able to accurately predict both ballistic limit velocity and residual velocity beyond the ballistic limit.
A GPU-based program was developed to accelerate the simulations of high velocity impact and to improve the performance of 3D SPH simulations, which are generally restrained by memory requirements. The SPH code development coupled to an efficient GPU algorithm provided promising results to investigate the interaction of two bodies in the context of high velocity impacts.

Acknowledgements

The author would like to thank Region Bourgogne-Franche-Comté, for its financial support. Computations have been performed on the supercomputer facilities of the Mésocentre de calcul de FrancheComté.

References

K A Alhussan, V A Babenko, I M Kozlov, and A S Smetannikov. Development of modified SPH approach for modeling of high-velocity impact. *International Journal of Heat and Mass Transfer*, 55:6340–6348, 2012.

Marvin E. Backman and Werner Goldsmith. The mechanics of penetration of projectiles into targets. *International Journal of Engineering Science*, 16(1):1–99, jan 1978. ISSN 0020-7225. doi: 10.1016/0020-7225(78)90002-2. URL https://www.sciencedirect.com/science/article/pii/0020722578900022.

T. Belytschko and I. S. Yeh. The splitting pinball method for contact-impact problems. *Computer Methods in Applied Mechanics and Engineering*, 105(3):375–393, jun 1993. ISSN 00457825. doi: 10.1016/0045-7825(93)90064-5. URL https://www.sciencedirect.com/science/article/pii/0045782593900645.

Ted Belytschko and Jerry I. Lin. A three-dimensional impact-penetration algorithm with erosion. *International Journal of Impact Engineering*, 5(1-4):111–127, jan 1987. ISSN 0734-743X. doi: 10.1016/0734-743X(87)90033-9. URL https://www.sciencedirect.com/science/article/pii/0734743X87900339.

T. Børvik, O.S. Hopperstad, T. Berstad, and M. Langseth. Numerical simulation of plugging failure in ballistic penetration. *International Journal of Solids and Structures*, 38(34-35):6241–6264, aug 2001a. ISSN 0020-7683. doi: 10.1016/S0020-7683(00)00343-7. URL https://www.sciencedirect.com/science/article/pii/S0020768300003437.

T Børvik, M Langseth, O.S Hopperstad, and K.A Malo. Perforation of 12 mm thick steel plates by 20 mm diameter projectiles with flat, hemispherical and conical noses: Part I: Experimental study. *International Journal of Impact Engineering*, 27(1):19–35, jan 2002. ISSN 0734-743X. doi: 10.1016/S0734-743X(01)00034-3. URL https://www.sciencedirect.com/science/article/pii/S0734743X01000343.

T. Børvik, S. Dey, and A.H. Clausen. Perforation resistance of five different high-strength steel plates subjected to small-arms projectiles. *International Journal of Impact Engineering*, 36(7):948–964, jul 2009. ISSN 0734-743X. doi: 10.1016/J.IJIMPENG.2008.12.003. URL https://www.sciencedirect.com/science/article/pii/S0734743X08003229.

Tore Børvik, John Rasmus Leinum, Jan Ketil Solberg, Odd Sture Hopperstad, and Magnus Langseth. Observations on shear plug formation in Weldox 460 E steel plates impacted by blunt-nosed projectiles. *International Journal of Impact Engineering*, 25(6):553–572, jul 2001b. ISSN 0734-743X. doi: 10.1016/S0734-743X(00)00069-5. URL https://www.sciencedirect.com/science/article/pii/S0734743X00000695.

Tore Børvik, Odd Sture Hopperstad, Magnus Langseth, and Kjell Arne Malo. Effect of target thickness in blunt projectile penetration of Weldox 460 E steel plates. *International Journal of Impact Engineering*, 28(4):413–464, apr 2003. ISSN 0734-743X. doi: 10.1016/S0734-743X(02)00072-6. URL https://www.sciencedirect.com/science/article/pii/S0734743X02000726.

J. Campbell, R. Vignjevic, and L. Libersky. A contact algorithm for smoothed particle hydrodynamics. *Computer Methods in Applied Mechanics and Engineering*, 184(1):49–65, mar 2000. ISSN 0045-7825. doi: 10.1016/S0045-7825(99)00442-9. URL https://www.sciencedirect.com/science/article/pii/S0045782599004429.

J. K. Chen, J. E. Beraun, and T. C. Carney. A corrective smoothed particle method for boundary value problems in heat conduction. *International Journal for Numerical Methods in Engineering*, 46(2):231–252, 1999. ISSN 00295981. doi: 10.1002/(SICI)1097-0207(19990920)46:2⟨231::AID-NME672⟩3.0.CO;2-K.

Andrea Colagrossi and Maurizio Landrini. Numerical simulation of interfacial flows by smoothed particle hydrodynamics. *Journal of Computational Physics*, 191(2):448–475, nov 2003. ISSN 00219991. doi: 10.1016/S0021-9991(03)00324-3. URL http://www.sciencedirect.com/science/article/pii/S0021999103003243.

Alejandro C. Crespo, Jose M. Dominguez, Anxo Barreiro, Moncho Gómez-Gesteira, and Benedict D. Rogers. Gpus, a new tool of acceleration in cfd: Efficiency and reliability on smoothed particle hydrodynamics methods. *PLOS ONE*, 6(6):1–13, 06 2011. doi: 10.1371/journal.pone.0020685. URL https://doi.org/10.1371/journal.pone.0020685.

S. Dey, T. Børvik, O.S. Hopperstad, J.R. Leinum, and M. Langseth. The effect of target strength on the perforation of steel plates using three different projectile nose shapes. *International Journal of Impact Engineering*, 30(8-9):1005–1038, sep 2004. ISSN 0734-743X. doi: 10.1016/J.IJIMPENG.2004.06.004. URL https://www.sciencedirect.com/science/article/pii/S0734743X04000971.

S. Dey, T. Børvik, X. Teng, T. Wierzbicki, and O.S. Hopperstad. On the ballistic resistance of double-layered steel plates: An experimental and numerical investigation. *International Journal of Solids and Structures*, 44(20):6701–6723, oct 2007. ISSN 0020-7683. doi: 10.1016/J.IJSOLSTR.2007.03.005. URL https://www.sciencedirect.com/science/article/pii/S0020768307001242.

J. M. Domìnguez, A. J. C. Crespo, M. Gómez Gesteira, and J. C. Marongiu. Neighbour lists in smoothed particle hydrodynamics. *International Journal for Numerical Methods in Fluids*, 67(12):2026–2042, 12 2011. ISSN 1097-0363. doi: 10.1002/fld.2481. URL https://doi.org/10.1002/fld.2481.

H. Frissane, L. Taddei, N. Lebaal, and S. Roth. Sph modeling of high velocity impact into ballistic gelatin. development of an axis-symmetrical formulation. *Mechanics of Advanced Materials and Structures*, 0(0):1–8, 2018. doi: 10.1080/15376494.2018.1452322. URL https://doi.org/10.1080/15376494.2018.1452322.

E. Giannaros, A. Kotzakolios, V. Kostopoulos, and G. Campoli. Hypervelocity impact response of CFRP laminates using smoothed particle hydrodynamics method: Implementation and validation. *International Journal of Impact Engineering*, 123:56–69, jan 2019. ISSN 0734-743X. doi: 10.1016/J.IJIMPENG.2018.09.016. URL https://www.sciencedirect.com/science/article/pii/S0734743X18305050.

R A Gingold and J J Monaghan. Smoothed particle hydrodynamics - Theory and application to non-spherical stars. *Monthly Notices of the Royal Astronomical Society*, 181:375–389, 1977. URL http://adsabs.harvard.edu/abs/1977MNRAS.181..375G.

N.K. Gupta, M.A. Iqbal, and G.S. Sekhon. Effect of projectile nose shape, impact velocity and target thickness on deformation behavior of aluminum plates. *International Journal of Solids and Structures*, 44(10):3411–3439, may 2007. ISSN 0020-7683. doi: 10.1016/J.IJSOLSTR.2006.09.034. URL https://www.sciencedirect.com/science/article/pii/S0020768306004045.

Colin J. Hayhurst and Richard A. Clegg. Cylindrically symmetric sph simulations of hypervelocity impacts on thin plates. *International Journal of Impact Engineering*, 20(1):337 – 348, 1997. ISSN 0734-743X. doi: https://doi.org/10.1016/S0734-743X(97)87505-7. URL http://www.sciencedirect.com/science/article/pii/S0734743X97875057. Hypervelocity Impact Proceedings of the 1996 Symposium.

Alexis Hérault, Giuseppe Bilotta, and Robert A. Dalrymple. Sph on gpu with cuda. *Journal of Hydraulic Research*, 48(sup1):74–79, 2010. doi: 10.1080/00221686.2010.9641247. URL https://doi.org/10.1080/00221686.2010.9641247.

M.A. Iqbal, A. Diwakar, A. Rajput, and N.K. Gupta. Influence of projectile shape and incidence angle on the ballistic limit and failure mechanism of thick steel plates. *Theoretical and Applied Fracture Mechanics*, 62:40 – 53, 2012. ISSN 0167-8442. doi: https://doi.org/10.1016/j.tafmec.2013.01.005. URL http://www.sciencedirect.com/science/article/pii/S0167844213000062.

Gordon R. Johnson and William H. Cook. A Constitutive Model and Data for Metals Subjected to Large Strains, High Strain Rates, and High Temperatures. *Proceedings 7th International Symposium on Ballistics*, pages 541–547, The Hague, 19-21 April 1983. ISSN 14710080.

Gordon R. Johnson and William H. Cook. Fracture characteristics of three metals subjected to various strains, strain rates, temperatures and pressures. *Engineering Fracture Mechanics*, 21(1):31–48, jan 1985. ISSN 0013-7944. doi: 10.1016/0013-7944(85)90052-9. URL https://www.sciencedirect.com/science/article/pii/0013794485900529.

Gordon R. Johnson and Robert A. Stryk. Eroding interface and improved tetrahedral element algorithms for high-velocity impact computations in three dimensions. *International Journal of Impact Engineering*, 5(1-4):411–421, jan 1987. ISSN 0734-743X. doi: 10.1016/0734-743X(87)90057-1. URL https://www.sciencedirect.com/science/article/pii/0734743X87900571.

L B Lucy. A numerical approach to the testing of the fission hypothesis. *The Astronomical Journal*, 82(12):1013–1024, 1977.

S Marrone, M Antuono, A Colagrossi, G Colicchio, D Le Touzé, and G Graziani. d -SPH model for simulating violent impact

flows. *Computer Methods in Applied Mechanics and Engineering*, 200(13-16):1526–1542, 2011. ISSN 0045-7825. doi: 10.1016/j.cma.2010.12.016. URL http://dx.doi.org/10.1016/j.cma.2010.12.016.

Vishal Mehra and Shashank Chaturvedi. High velocity impact of metal sphere on thin metallic plates: A comparative smooth particle hydrodynamics study. *Journal of Computational Physics*, 212(1):318–337, 2006. ISSN 00219991. doi: 10.1016/j.jcp.2005.06.020. URL http://www.sciencedirect.com/science/article/pii/S0021999105003232.

Athanasios Mokos, Benedict D. Rogers, Peter K. Stansby, and José M. Domínguez. Multi-phase sph modelling of violent hydrodynamics on gpus. *Computer Physics Communications*, 196:304 – 316, 2015. ISSN 0010-4655. doi: https://doi.org/10.1016/j.cpc.2015.06.020. URL http://www.sciencedirect.com/science/article/pii/S0010465515002659.

J J Monaghan. SPH without a tensile instability. *Journal of Computational Physics*, 159(2):290–311, 2000.

J J Monaghan and R A Gingold. Shock simulation by the particle method SPH. *Journal of Computational Physics*, 52(2):374–389, nov 1983. ISSN 00219991. doi: 10.1016/0021-9991(83)90036-0. URL http://adsabs.harvard.edu/abs/1983JCoPh..52..374M.

Simon Pabst, Artur Koch, and Wolfgang Straßer. Fast and scalable CPU/GPU collision detection for rigid and deformable surfaces. *Eurographics Symposium on Geometry Processing*, 29(5):1605–1612, 2010. ISSN 17278384. doi: 10.1111/j.1467-8659.2010.01769.x.

P.W. Randles and L.D. Libersky. Smoothed particle hydrodynamics: Some recent improvements and applications. *Computer Methods in Applied Mechanics and Engineering*, 139(1):375 – 408, 1996. ISSN 0045-7825. doi: https://doi.org/10.1016/S0045-7825(96)01090-0. URL http://www.sciencedirect.com/science/article/pii/S0045782596010900.

Bo Ren and Shaofan Li. Meshfree simulations of plugging failures in high-speed impacts. *Computers & Structures*, 88(15-16):909–923, aug 2010. ISSN 0045-7949. doi: 10.1016/J.COMPSTRUC.2010.05.003. URL https://www.sciencedirect.com/science/article/pii/S0045794910001173.

Amit Shaw and S.R. Reid. Heuristic acceleration correction algorithm for use in sph computations in impact mechanics. *Computer Methods in Applied Mechanics and Engineering*, 198(49):3962 – 3974, 2009. ISSN 0045-7825. doi: https://doi.org/10.1016/j.cma.2009.09.006. URL http://www.sciencedirect.com/science/article/pii/S0045782509003041.

Amit Shaw, D. Roy, and S.R. Reid. Optimised form of acceleration correction algorithm within sph-based simulations of impact mechanics. *International Journal of Solids and Structures*, 48(25):3484 – 3498, 2011. ISSN 0020-7683. doi: https://doi.org/10.1016/j.ijsolstr.2011.09.003. URL http://www.sciencedirect.com/science/article/pii/S0020768311003039.

S Swaddiwudhipong, M J Islam, and Z S Liu. High velocity penetration/peforation using coupled smooth particle hydrodynamics-finite elements method. *International journal of protective structures*, 1(4), 2010.

L Taddei, A Awoukeng Goumtcha, and S Roth. Smoothed Particle Hydrodynamics Formulation for Penetrating Impacts on Ballistic gelatine. *Mechanics Research Communications*, 70:94–101, sep 2015. ISSN 00936413. doi: 10.1016/j.mechrescom.2015.09.010. URL http://www.sciencedirect.com/science/article/pii/S0093641315001597.

R Vignjevic and J Campbell. A penalty approach for contact in smoothed particle hydrodynamics. *International Journal of Impact Engineering*, 23(1):945–956, 1999. ISSN 0734743X. doi: 10.1016/S0734-743X(99)00137-2. URL http://www.sciencedirect.com/science/article/pii/S0734743X99001372.

Rade Vignjevic, James Campbell, and Severine Lepage. Numerical Simulation of High Velocity Impact on Thin Metalic targets I and II. 2004.

Z.L. Zhang and M.B. Liu. Smoothed particle hydrodynamics with kernel gradient correction for modeling high velocity impact in two- and three-dimensional spaces. *Engineering Analysis with Boundary Elements*, 83:141–157, oct 2017. ISSN 0955-7997. doi: 10.1016/J.ENGANABOUND.2017.07.015. URL https://www.sciencedirect.com/science/article/pii/S0955799717301261.

Jingwei Zheng, Xuehui An, and Miansong Huang. GPU-based parallel algorithm for particle contact detection and its application in self-compacting concrete flow simulations. *Computers & Structures*, 112-113:193–204, dec 2012. ISSN 0045-7949. doi: 10.1016/J.COMPSTRUC.2012.08.003. URL https://www.sciencedirect.com/science/article/pii/S0045794912001915.